IEEE Journal of
Microwaves

Received 12 June 2024; revised 27 July 2024 and 12 August 2024; accepted 10 September 2024. Date of publication 30 September 2024;
date of current version 9 October 2024.

Digital Object Identifier 10.1109/JMW.2024.3459909

A D-Band Self-Packaged Low Loss Grounded Coplanar Waveguide to Rectangular Waveguide Transition With Silicon-Based Air Cavity-Backed Structure

ZI-QI ZHANG [1] **(Graduate Student Member, IEEE), XIAO-LONG HUANG** [2] **(Senior Member, IEEE),**
LIANG ZHOU [1] **(Senior Member, IEEE), YIN-SHAN HUANG** [1] **(Member, IEEE),**
AND CHENG-RUI ZHANG [1] **(Member, IEEE)**

(Regular Paper)

[1] State Key Laboratory of Radio Frequency Heterogeneous Integration, Shanghai Jiao Tong University, Shanghai 200240, China
[2] Department of Electrical and Computer Engineering, Princeton University, Princeton, NJ 08540 USA

CORRESPONDING AUTHOR: Liang Zhou (e-mail: liangzhou@sjtu.edu.cn).

This work was supported in part by the National Key Research and Development Project under Grant 2023YFB4403802; in part by the National Natural Science Foundation of China under Grant 62325110 and Grant 62188102; and in part by Shenzhen Science and Technology Program under Grant KQTD20221101093555005.

ABSTRACT A novel D-band self-packaged silicon-based air cavity-backed transition from grounded coplanar waveguide to air-filled rectangular waveguide was investigated, fabricated, and measured in this work. The equivalent circuit model was established and analyzed in detail, and design procedures are given. The calculated, simulated, and measured S-parameters of the transition show some agreement. The minimum measured insertion loss of the proposed transition is 1.1 dB at 147 GHz with a fractional 3-dB bandwidth of 10.2%. This transition demonstrates outstanding performance of low loss and profile compared with state-of-the art works in our in-house silicon-based MEMS photosensitive composite film fabrication process. It can be further used in a high-performance joint radar communication system in packaging.

INDEX TERMS Benzocyclobutene (BCB), self-packaged, transition, MEMS, silicon-based, low loss, system in packaging, cavity-backed, through silicon ring trench (TSRT), D-band.

I. INTRODUCTION

Millimeter-wave/Sub-terahertz radar sensor [1], [2] and wireless backhaul system [3], [4] have been extensively investigated in recent years. The joint radar communication system at D-band has advantages of resolution and wireless transmission speed because of its wide relative bandwidth [5], [6]. However, interconnection loss in this sub-terahertz system is usually high using wire bonding [7], thus being the main bottleneck and limiting the performance of the radar and communication system. Therefore, a low-loss, low-cost, and compact transition between the transceiver and antenna is highly in demand.

Planar transitions, such as slot radiator or tapered structure [8], [9], [10], suffer from high insertion loss with large size. Non-galvanic interface transition [11], [12] is able to provide low-loss transmission. However, high alignment accuracy is usually required, which increases system integration complexity. Furthermore, a series of substrate integrated waveguide (SIW)-to-rectangular waveguide (RWG) transitions utilizing stepped impedance transformer or aperture coupled patch [13], [14], [15] have been demonstrated because they have a relatively wide bandwidth and compact size. However, they are often used below 110 GHz.

Packaging technology becomes increasingly crucial in wireless systems. 3D interconnections, such as flip-chip and embedded wafer level ball (eWLB) grid array [16], [17], [18], [19], [20], have been investigated because of high-density integration in the sub-terahertz band. However, heat dissipation and energy leakage through the non-galvanic coupled structure are the major challenges because of the large size of the ball grid array.

Nowadays, high-performance interconnections between transceiver to waveguide in the sub-terahertz band still face challenges because integration and ease of fabrication process must be considered in a chip-to-waveguide transition design. Recently, low-loss transitions in the glass substrate utilizing laser-induced deep etching technology [21], [22] and on-chip transitions [23], [24] have been investigated. Nevertheless, these concepts using dielectric waveguide with multilayer technology or using electromagnetic bandgap (EBG) structure increase the strict requirement of precise alignment and have a relatively large size.

Recently, various heterogeneous integrated passive components like filter or antenna and radar systems have been demonstrated by using our in-house silicon-based MEMS photosensitive composite film fabrication process [25], [26], [27]. Several reported packaging methods in recent years have been compared. Benzocyclobutene (BCB) has some advantages because of its low dielectric constant and dissipation factor. The loss of the BCB-based GCPW is less than 0.3 dB/mm and the loss of a via is only 0.15 dB at 94 GHz [28]. This interconnection loss is much better than that of eWLB (1 dB per ball) and wire bonding (1.5–2.5 dB) in the W band [29].

In this paper, a D-band low-loss 3D silicon-based air cavity-backed transition was investigated, fabricated, and measured. This paper is an expansion of [30], which only studies the mechanism of the coupled aperture in transmission and is partly repeated in Section II of this paper. The transition with bulky size in [30] is prone to the risk of fracture during fabrication process, which reduces the yield of the sample. The equivalent circuit model was established and analyzed to verify the operating mechanism, and design procedures were given. To the best of our knowledge, this transition has lower insertion loss compared with state-of-the art works. This transition can be further interconnected with a D-band joint radar communication CMOS transceiver [31] and antenna to demonstrate a high-performance system in packaging by using our silicon-based MEMS photosensitive composite film fabrication process as shown in Fig. 1.

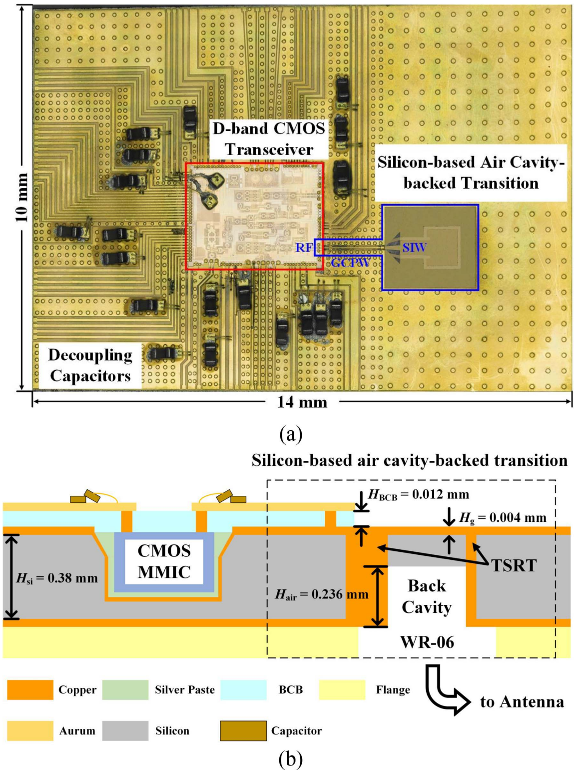

FIGURE 1. (a) Photograph and (b) cross view of the joint radar communication system in packaging with our proposed silicon-based air cavity-backed transition at D-band.

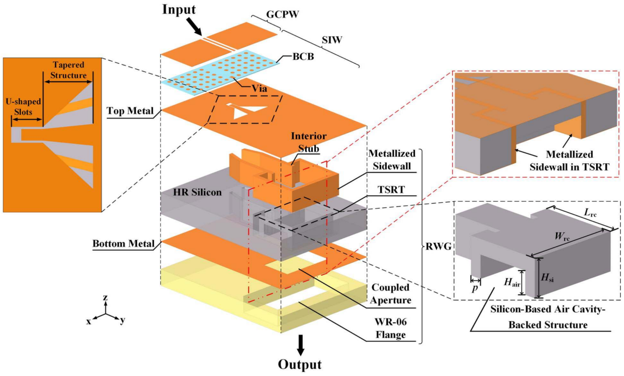

FIGURE 2. The 3D silicon-based air cavity-backed transition from the embedded MMIC to WR-06 waveguide.

II. SILICON-BASED AIR CAVITY-BACKED TRANSITION AND ITS EQUIVALENT CIRCUIT MODEL

A. STRUCTURE OF THE SILICON-BASED AIR CAVITY-BACKED TRANSITION

The proposed silicon-based air cavity-backed transition consists of grounded coplanar waveguide (GCPW)-to-SIW and SIW-to-RWG, as shown in Fig. 2. RF signal is transmitted from the GCPW to the SIW through a taper by using a rectangular hole.

Fig. 3 shows the geometry of the GCPW-to-SIW transition. The length of the taper is initially set to $\lambda_g/2$ for impedance matching and bandwidth, where the λ_g is the guided wavelength at the operating frequency. The photosensitive composite film (BCB) is used in the GCPW as a substrate where the thickness is $H_{BCB} = 12$ um with a dielectric constant of $\varepsilon_r = 2.65$ and dissipation factor tanδ of 0.0008.

Fig. 4 shows the simulated electric field distributions and magnetic field vector direction of the GCPW-to-SIW where the TEM mode is in the GCPW and the TE_{10} mode is in the SIW. Two parallel U-shaped slots are designed to enhance the coupling with its initial length $\lambda_g/4$.

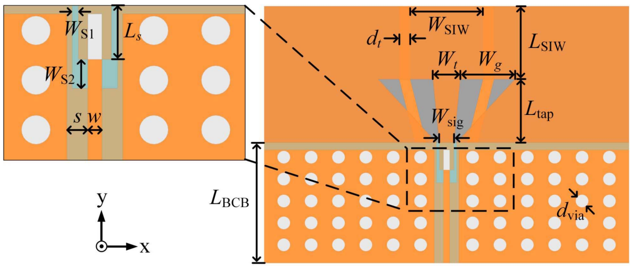

FIGURE 3. Geometry of the GCPW-to-SIW transition.

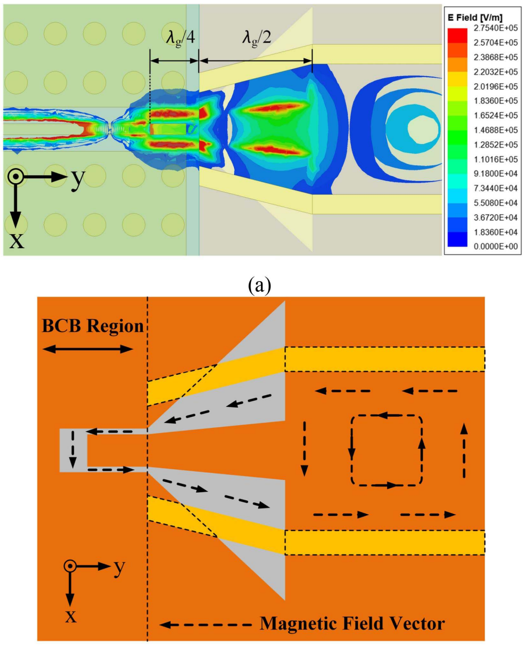

(a)

(b)

FIGURE 4. (a) Electric field distributions and (b) magnetic field vector direction of the GCPW-to-SIW transition at 152.5 GHz.

Fig. 5 shows the geometry of the SIW-to-RWG transition. R_x and R_y are the length and width of the rectangular waveguide in the output, respectively. m and n are the length and width of the air cavity-backed structure, respectively. W_{rc} and L_{rc} represent the width and length of the through silicon ring trench (TSRT). The TSRT is designed to realize vertical transmission. Fig. 6 illustrates the electromagnetic field distributions. The silicon-based air cavity-backed structure couples the energy from the resonator to the air-filled rectangular waveguide. The bottom of the back cavity is reached at the maximum field strength to ensure adequate coupling through the broad edges.

B. EQUIVALENT CIRCUIT MODEL

An equivalent circuit of the silicon-based-air cavity-backed transition is shown in Fig. 7 and is divided into two parts. The first part is represented by the *ABCD* matrix through

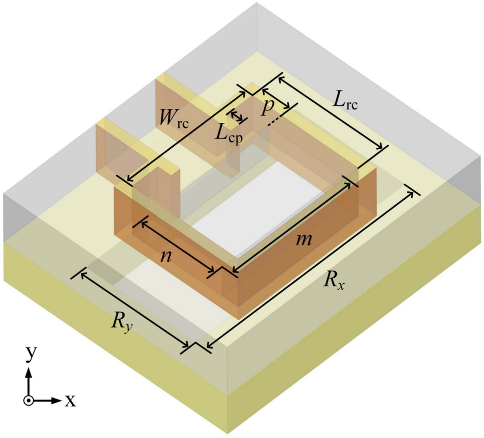

FIGURE 5. Geometry of the SIW-to-RWG transition.

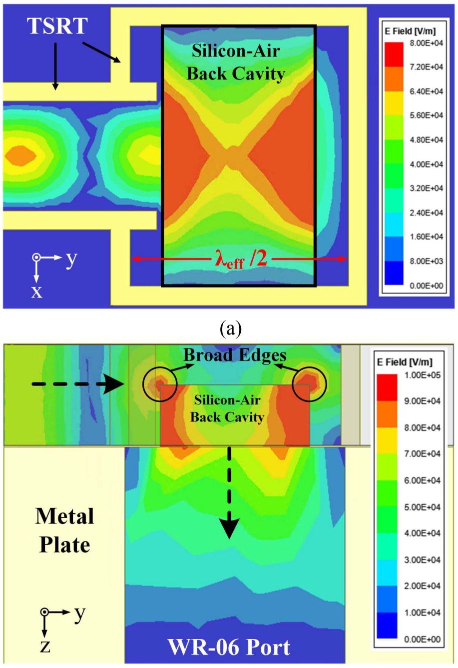

(a)

(b)

FIGURE 6. Electric field distributions of SIW-to-RWG. (a) Top and (b) cross section view.

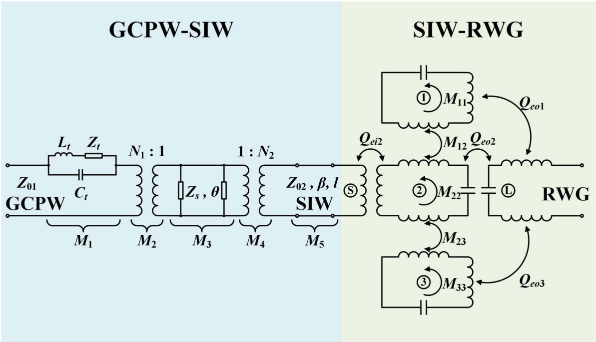

FIGURE 7. Equivalent circuit model of the proposed silicon-based air cavity-backed transition.

multiplying five cascaded submatrices, and the second part is indicated by a coupling matrix.

M_1 represents the rectangular hole (from GCPW to taper) which consists of a parasitic inductor L_t, a resistor Z_t, and a capacitor C_t in parallel. M_3 represents the U-shaped slot and taper, which consists of a resistor Z_s with an electrical length θ. M_2 and M_4 are transformers that mutually couple with the ratios N_1 and N_2 referenced to [32]. M_5 is the SIW with a length of l and propagation constant of β. Z_{01} and Z_{02} are the characteristic impedance of the GCPW and SIW, respectively. Therefore, the *ABCD* matrix can be calculated as

$$M = M_1 M_2 M_3 M_4 M_5 = \begin{bmatrix} A & B \\ C & D \end{bmatrix} \tag{1}$$

where

$$A = \left(\frac{N_1}{N_2} + \frac{2X}{jN_1 N_2 Z_s \tan\theta} \right) \cos\beta l + \frac{jN_2 X \sin\beta l}{N_1 Z_{02}} \tag{2}$$

$$B = \left(\frac{N_1}{N_2} + \frac{2X}{jN_1 N_2 Z_s \tan\theta} \right) jZ_{02} \sin\beta l + \frac{N_2 X}{N_1} \cos\beta l \tag{3}$$

$$C = \frac{2}{jN_1 N_2 Z_s \tan\theta} \cos\beta l + \frac{N_2}{N_1} \frac{j \sin\beta l}{Z_{02}} \tag{4}$$

$$D = \frac{2}{jN_1 N_2 Z_s \tan\theta} jZ_{02} \sin\beta l + \frac{N_2}{N_1} \cos\beta l \tag{5}$$

$$X = \frac{j\omega L_t + Z_t}{1 - \omega^2 L_t C_t + j\omega Z_t C_t} \tag{6}$$

The input and output characteristic impedance of the GCPW-to-SIW are not equal. The *ABCD* matrix to *S* matrix of the GCPW-to-SIW can be calculated by using (7)–(10). The S-parameters of the GCPW-to-SIW can be obtained by substituting (2)–(6) into (7)–(10).

$$S'_{11} = \frac{AZ_{02} + B - CZ_{02}Z_{01} - DZ_{01}}{AZ_{02} + B + CZ_{02}Z_{01} + DZ_{01}} \tag{7}$$

$$S'_{12} = \frac{2\sqrt{Z_{01}Z_{02}}\,(AD - BC)}{AZ_{02} + B + CZ_{02}Z_{01} + DZ_{01}} \tag{8}$$

$$S'_{21} = \frac{2\sqrt{Z_{01}Z_{02}}}{AZ_{02} + B + CZ_{02}Z_{01} + DZ_{01}} \tag{9}$$

$$S'_{22} = \frac{-AZ_{02} + B - CZ_{02}Z_{01} + DZ_{01}}{AZ_{02} + B + CZ_{02}Z_{01} + DZ_{01}} \tag{10}$$

Fig. 8 shows the calculated S-parameters using (7) and (9). The initial frequency is set to be 150 GHz. Fig. 8(a) depicts the resonant frequency increases with the parasitic inductance L_t and capacitance C_t increasing. The circuit model without parasitics ($C_t = \infty$ nF, $L_t = 0$ pH) resonates at the initial frequency point because of the initial length of the slotline. The influence of parasitic parameters changes the theoretical resonant frequency. Fig. 8(b) shows that increasing turn ratios and normalized impedance improve the resonant frequency and bandwidth.

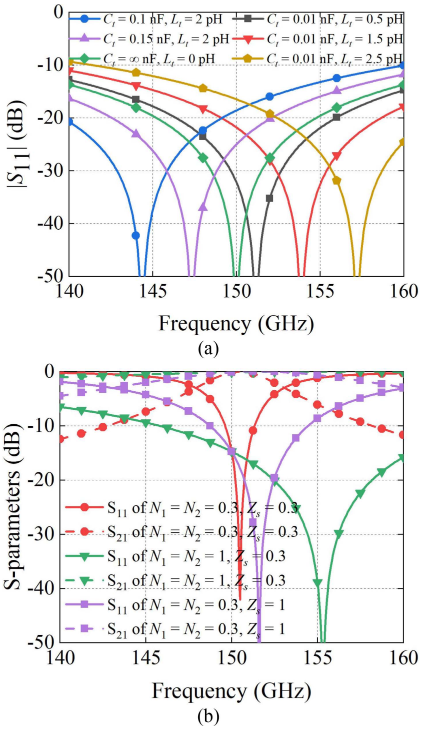

(a)

(b)

FIGURE 8. Calculated S-parameters of the equivalent circuit depending on variation of (a) extracted inductance and capacitance when $N_1 = N_2 = 1$ and $Z_s = 0.5$, and (b) turn ratios and normalized impedance when $C_t = 0.05$ nF and $L_t = 1$ pH.

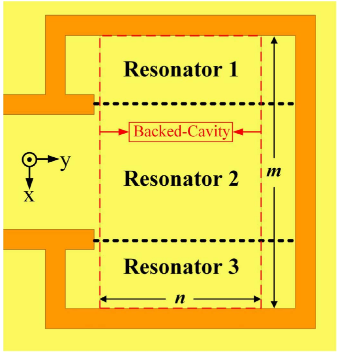

FIGURE 9. Diagram of the SIW-to-RWG.

The SIW-to-RWG structure can be divided into three resonators, as shown in Fig. 9. The equivalent circuits, therefore, consist of three resonators, as shown in Fig. 7. Q_{ei2} denotes the external quality factor from SIW to resonator 2. Q_{eo1}, Q_{eo2}, and Q_{eo3} denote the external quality factors from the three resonant cavities to the output, respectively. The mutual coupling coefficients M_{12} and M_{23} stand for the magnetic coupling between resonators. M_{11}, M_{22} and M_{33} denote the self-coupling coefficients. The coupling mechanism is symmetrical and asynchronous according to the unique topology as shown in Fig. 9. The coupling matrix $[m]$ of the SIW-to-RWG can be expressed as

$$[m] = \begin{bmatrix} 0 & 0 & 0.94 & 0 & 0 \\ 0 & 0.86 & 0.55 & 0 & 0.58 \\ 0.94 & 0.55 & -0.35 & 0.55 & -0.65 \\ 0 & 0 & 0.55 & 0.86 & 0.58 \\ 0 & 0.58 & -0.65 & 0.58 & 0 \end{bmatrix} \tag{11}$$

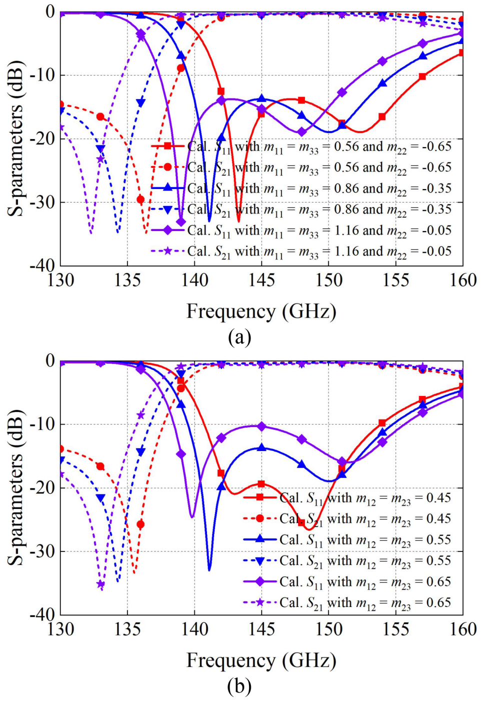

(a)

(b)

FIGURE 10. **Calculated S-parameters from the coupling matrix versus (a) self-coupling and (b) mutual coupling coefficients.**

Therefore, the S-parameters of the SIW-to-RWG transition can be represented by S''_{11} and S''_{21} from [33] by utilizing the extracted coupling matrix. Fig. 10 shows the calculated S-parameters using the extracted coupling matrix with the variation of coupling coefficients. The frequencies of transmission zero and the center frequency decrease with self-coupling coefficients increasing. The calculated bandwidth of the SIW-to-RWG transition increases, while the center frequency remains unchanged when the mutual coupling coefficients increasing.

Finally, the theoretical S-parameters of the equivalent circuit model of the silicon-based air backed-cavity transition in Fig. 7 can be calculated by cascading two-port networks as

$$\begin{cases} S_{11} = S'_{11} + kS'_{12}S'_{21}S''_{11} \\ S_{21} = kS'_{21}S''_{21} \end{cases} \tag{12}$$

where k is derived as

$$k = \frac{1}{1 - S'_{22}S''_{11}} \tag{13}$$

III. DESIGN PROCEDURE OF THE SILICON-BASED AIR CAVITY-BACKED TRANSITION

The silicon-based air cavity-backed transition is designed in D-band as an example. The bandwidth is set to 11% with its center frequency at 147 GHz. The air-filled waveguide is WR-06 flange with a size of 1.651 × 0.8255 mm^2 at D-band. The high-resistivity silicon with a dielectric constant of $\varepsilon_r = 11.6$ and dissipation factor tanδ of 0.0002 is used as the substrate.

The design procedures are summarized as follows:

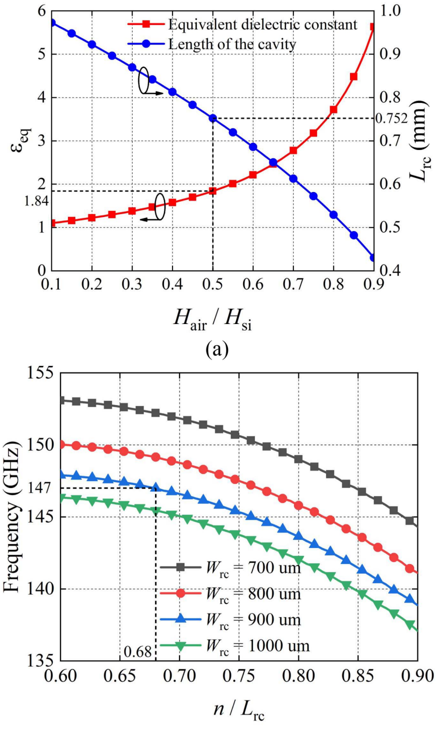

(a)

(b)

FIGURE 11. **(a) Equivalent dielectric constant ε_{eq} and cavity length versus the thickness ratio H_{air}/H_{si} by choosing different H_{air}. (b) Resonant frequency of the TE$_{121}$ mode versus length ratio n/L_{rc} at different cavity width W_{rc} with a fixed cavity length.**

1) The transition from GCPW to SIW is designed. The thickness (H_{si}) of the silicon substrate is set to 380 μm in this study for the machinable aspect ratio of the TSRT structure. The SIW width (W_{SIW}) is set to guarantee the fundamental mode (TE$_{10}$) in the transition. The initial length of the slot line (L_s) and the length of the tapered structure (L_{tap}) are set to $\lambda_g/4$ and $\lambda_g/2$, respectively, at the operating frequency.
2) The SIW to RWG structure is designed. The original thickness ratio (H_{air}/H_{si}) is set to 0.5 based on the field analysis in Fig. 5. The cavity length (L_{rc}) is approximately $\lambda_{eff}/2$ which is 0.752 mm in this case. λ_{eff} is the guided wavelength corresponding to the equivalent dielectric constant ε_{eq} simplified from [34]. The equivalent dielectric constant ε_{eq} and the length (L_{rc}) versus the thickness of the cavity to the silicon substrate (H_{air}/H_{si}) are shown in Fig. 11(a). If the initial width (W_{rc}) is 900 μm, n/L_{rc} = 0.68, then, the initial length (n) is 510 μm where TE$_{121}$ mode is operated. The ratio (n/L_{rc}) with different width versus frequency (W_{rc}) is shown in Fig. 11(b).
3) The self-coupling coefficients can be obtained from Fig. 12(a) where $m_{11} = m_{33} = 0.91$ and $m_{22} = -0.3$. The height H_{air} is finally set to 235 μm at 147 GHz. The mutual coupling coefficients $m_{12} = m_{23} = 0.55$ can be obtained if the bandwidth is 11%, as shown in

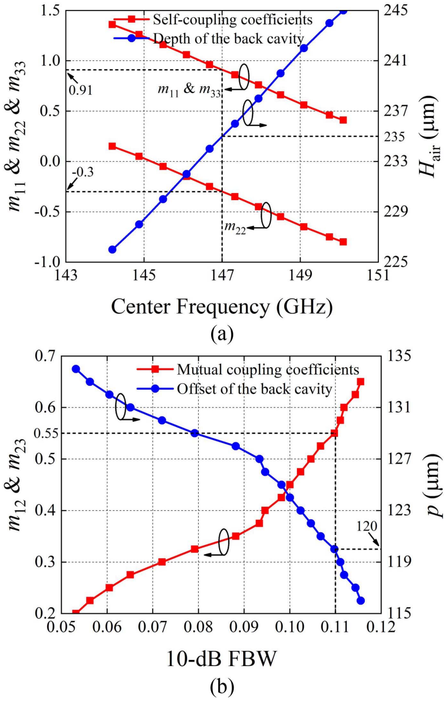

FIGURE 12. (a) Self-coupling coefficients m_{11}, m_{22}, and m_{33} versus the center frequency corresponding to H_{air}. (b) Mutual coupling coefficients m_{12} and m_{23} versus 10 dB fractional bandwidth corresponding to the offset p.

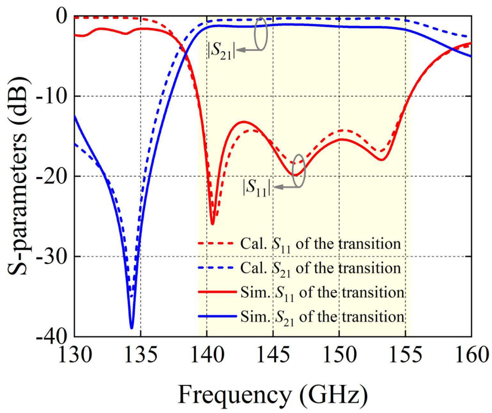

FIGURE 13. Comparisons of S-parameters of the proposed transition using equivalent circuit model and simulation results by HFSS.

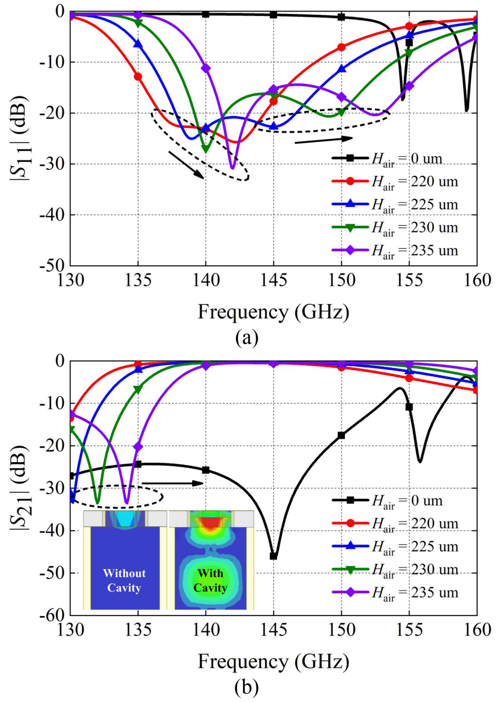

FIGURE 14. Simulated S-parameters versus the height of the air cavity (a) S_{11} and (b) S_{21}.

TABLE 1. Parameters of the Proposed Transition

DIMENSION (mm)					
GCPW	w	0.034	SIW	L_{SIW}	0.6
	s	0.0506		L_t	0.347
	d_{via}	0.07		W_{SIW}	0.4
	L_{BCB}	0.6		d_t	0.07
U-SHAPED SLOT LINE	W_{S1}	0.015	TAPERED SLOT LINE	W_{sig}	0.08
	W_{S2}	0.07		W_t	0.14
	L_S	0.15		W_g	0.34
BACKED CAVITY	W_{rc}	0.95	WR-06	R_x	1.651
	L_{rc}	0.8		R_y	0.8255
	p	0.12	THICKNESS	H_{BCB}	0.012
	L_{cp}	0.1		H_{air}	0.236
	m	0.95		H_{si}	0.38
	n	0.56		H_g	0.004

Fig. 12(b). In that case, the offset (p) is set to 120 μm. Finally, the parameters of the silicon-based air cavity-backed transition are optimized by tuning the resonant cavity surrounded by TSRT.

Fig. 13 presents the comparisons between the calculated and simulated S-parameters of the transition. Agreement can be observed. The center frequency is 147.2 GHz with the 10-dB bandwidth of 16 GHz. The simulated insertion loss is 1.05 dB at 146 GHz.

Fig. 14 shows the simulated SIW-to-RWG transmission performance with different heights to verify the design procedure by using HFSS. The bandwidth increases and moves toward high frequency if H_{air} increases because the effective dielectric constant is decreasing. The electromagnetic energy will not radiate into the rectangular waveguide if $H_{\mathrm{air}} = 0$. Table 1 lists the dimensions of the silicon-based air cavity-backed transition.

IV. FABRICATION PROCESS OF THE PROPOSED TRANSITION

Fig. 15 shows the fabrication process of the proposed self-packaged silicon-based air cavity-backed transition. A 4-inch 500 μm thick high-resistivity silicon wafer with a 300 nm

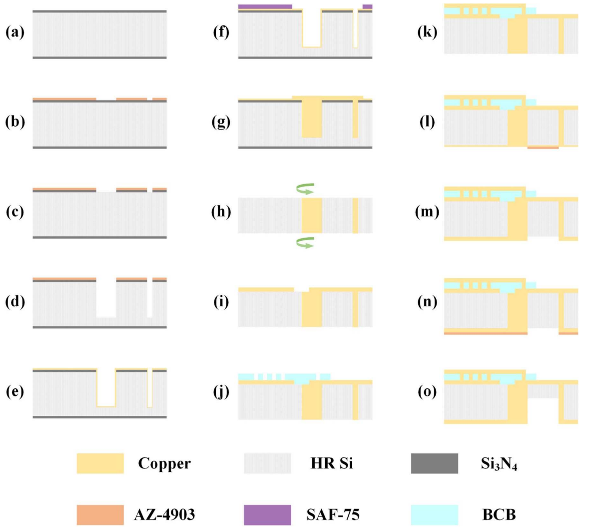

FIGURE 15. Fabrication process of the proposed self-packaged silicon-based air cavity-backed transition. (a) A 500 μm thick high-resistivity silicon wafer with Si_3N_4 deposited on both sides. (b) Spin coating photoresist AZ-4903. (c) Removing the unprotected part of Si_3N_4. (d) Fabricating TSRT. (e) Sputtering the Cr/Cu seed layer. (f) Spin coating dry-film photoresist SAF-75. (g) Electroplating Cu. (h) Mechanical grinding and polishing. (i) Metallizing the ground layer. (j) Spin coating BCB layer. (k) Metallizing the top layer. (l) Sputtering the Cr/Cu seed layer and spin coating AZ-4903 on the back side. (m) Metallizing the bottom metal layer. (n) Spin coating 12 μm thick AZ-4903. (o) Backside etching and rinsing.

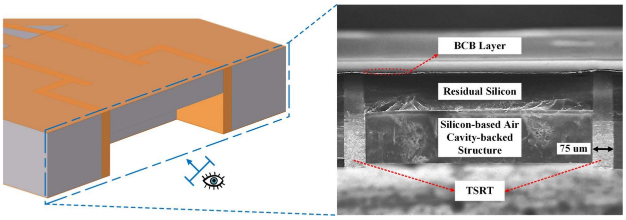

FIGURE 16. SEM image of the profile at the silicon-based air cavity-backed section of the transition with TSRT structure inside the silicon wafer.

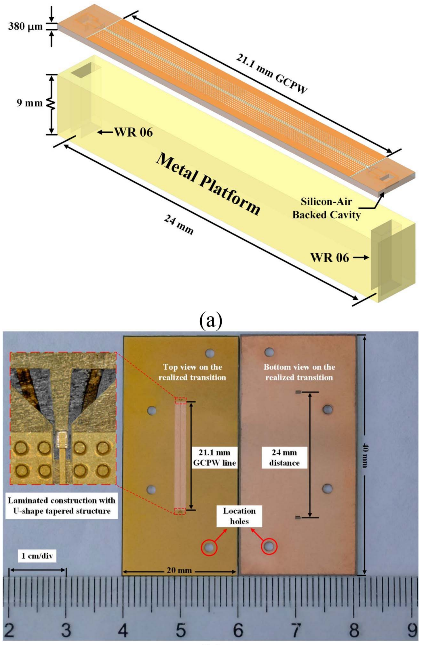

(a)

(b)

FIGURE 17. (a) Structure and (b) photograph of the back-to-back transition.

thick Si_3N_4 layer deposited on both sides is used as a carrier of the transition (Fig. 15(a)). The positive photoresist AZ-4903 is spin coated as a mask of the TSRT structure, followed by etching the unprotected part of Si_3N_4 using ion-beam etching technology (Fig. 15(b)–(c)). Fig. 15(d) shows the dry etching process to fabricate the TSRT structure. The Cr/Cu seed layers are sputtered on the front side of the wafer, as shown in Fig. 15(e). The dry-film photoresist SAF-75 is then deposited on the surface as a mask to prevent impurity from entering the ring trench (Fig. 15(f)). The exposed TSRT structure is electroplated in the electroplate liquid, which has the function of accelerating the metallization process in the ring trench and inhibiting the growth of the surface metal layer (Fig. 15(g)). Fig. 15(h) shows the mechanical grinding and polishing process using the automatic surface grinder DAG810 to remove the raised Cu layer. The polishing process reduces the roughness of the wafer surface, which helps decrease the transmission loss.

Fig. 15(i) shows the metallization of the ground layer to form U-shaped slots and a tapered slot line on the front side. The 12 μm thick photosensitive composite thin-film BCB is spin coated above the metal layer to serve as the redistribution layer, as shown in Fig. 15(j). The Cu layer is electroplated on the top after sputtering and lithography, as shown in Fig. 15(k). In Fig. 15(l), the Cr/Cu seed layer with the same parameters is sputtered on the back side. After electroplating, ion beam etching is performed in the bottom metal layer by using argon as shown in Fig. 15(m). A photoresist AZ-4903 is spin coated again to expose the aperture portion of the silicon for deep silicon etching (Fig. 15(n)). Finally, the silicon-based air cavity-backed structure is fabricated by using localized backside etching with the Bosch DRIE process, and the wafer is rinsed with acetone, as shown in Fig. 15(o).

As shown in Fig. 16, the silicon-based air cavity-backed structure with the depth of 236 μm is formed. The TSRT is filled with electroplated Cu without any void inside and is almost perpendicular to the horizontal plane. The flatness of the residual silicon surface reflects the uniformity of DRIE process. The width of the TSRT is 75 μm, which is within a reasonable tolerance of geometric deformation from the designed parameters.

V. MEASUREMENT RESULTS AND DISCUSSION

Fig. 17(a) shows a back-to-back transition because GCPW to RWG cannot be directly measured due to the difficulty of calibration in the millimeter wave. The length of the back-to-back transition is 24 mm, where the length of the GCPW is 21.1 mm. Each silicon-based air cavity-backed transition has a

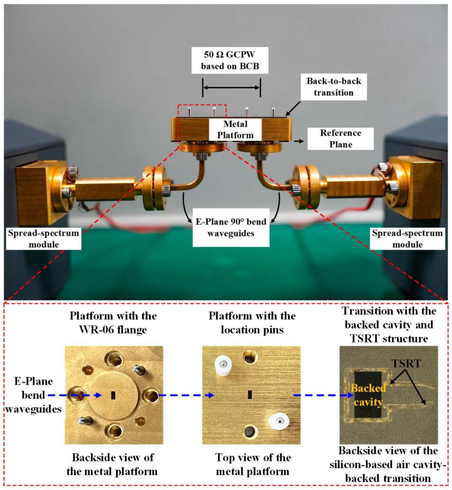

FIGURE 18. Photograph of the measurement setup for the proposed transition.

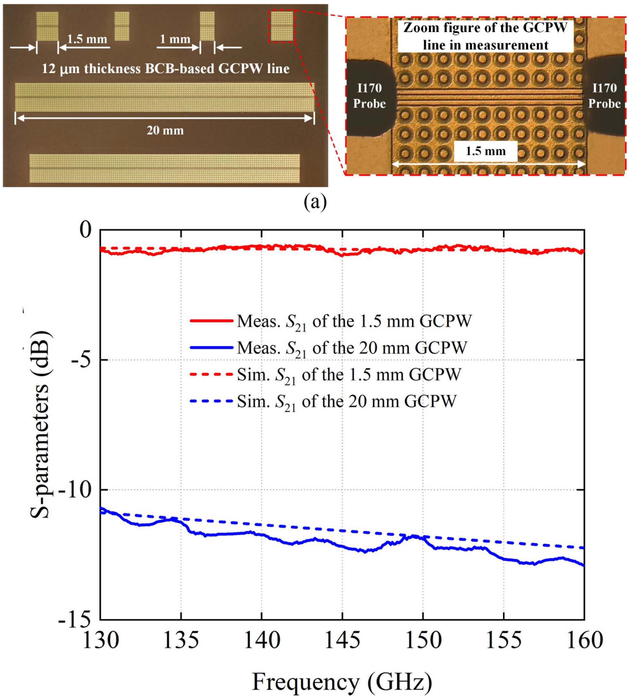

(a)

(b)

FIGURE 19. (a) Photo of the BCB-based GCPW with the zoom figure of measurement detailed in the right, and (b) measured S-parameters of the 1.5 and 20 mm BCB-based GCPW from 130 GHz to 160 GHz.

length of 0.55 mm BCB-based GCPW transmission line. The thickness of the silicon substrate is 380 μm. The transition is then mounted on a 9 mm height metal platform with two rectangular waveguides (WR-06) on both sides. Fig. 17(b) shows the photo of the back-to-back transition.

Fig. 18 shows the photograph of the measurement setup. It includes a Rohde & Schwarz ZVA-67 vector network analyzer (VNA) with two spread-spectrum modules. The setup also contains a metal platform to fix the sample and a pair of standard E-Plane90° bend waveguides. Four locating holes are used for aligning with the WR-06 flange. The transmission path from the backside of the metal platform to the proposed transition has been exhibited in the zoom figure. The measurement is calibrated at the end of two E-Plane bend waveguides by utilizing the D-band TRL calibration kit.

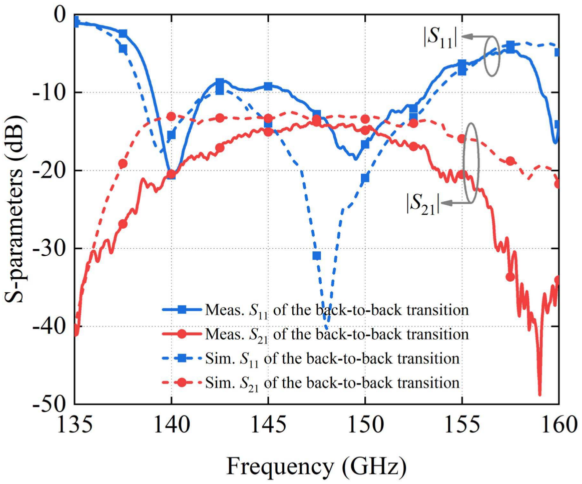

FIGURE 20. Comparisons between the simulated and measured results of the back-to-back transition.

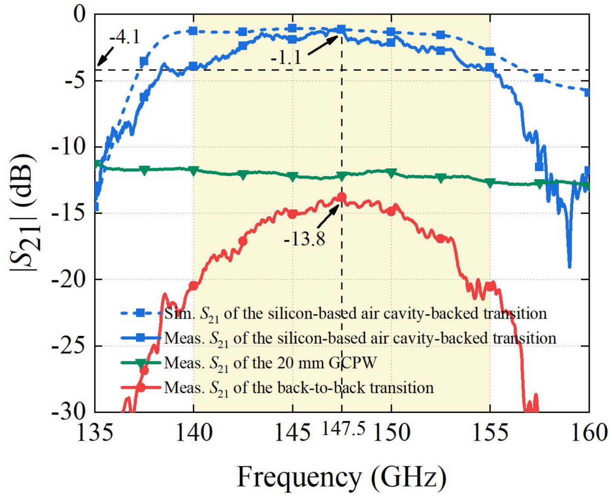

FIGURE 21. Simulated and measured insertion loss of the back-to-back transition, 20 mm long BCB-based GCPW, and the compensated insertion loss of each silicon-based air cavity-backed transition.

Fig. 19(a) shows the photo of the different length of the BCB-based GCPW. A pair of Infinity probes I170 are used in the 1.5 and 20 mm GCPW measurement at D-band. Fig. 19(b) shows the simulated and measured S-parameters of the 1.5 and 20 mm BCB-based GCPW from 130 GHz to 160 GHz where the surface roughness of the metal layer is 470 nm and the fabrication tolerance is considered. The measured insertion loss of the 1.5 and 20 mm GCPW are 0.87 dB and 11.6 dB at 145 GHz, respectively. Therefore, the attenuation

TABLE 2. Comparison of the State-of-the-Art Microstrip/GCPW-to-Waveguide Transitions

Ref.	Frequency Band (GHz)	Design Technique	Substrate Material (ε_r)	Insertion Loss (dB)	3-dB FBW (%)	Lateral Dimension (λ_0×λ_0)##	Thickness (λ_0)##	Fabrication Technology	Complexity Level	Transition Type
[7]	111–133	Wirebonding	Polytec TC430-T 3.185	2.21†	17.4	N/A	0.31	QFN	Medium	CPW-Bond Wires-MSL
[8]	135–160	Slot Radiator	Silicon Dioxide 4	4.2	16.9	0.93×0.46	0.42	SiGe	Low	MSL-RWG
[9]	122–156	Metal Ridge	Quartz 3.9	<2	24.5	1.67×1.12	0.45	MEMS	Low	CPW-RWG
[10]	105–135	Tapered Structure	RO 3003 RO 5880 2.25	1.2	25*	3.2×1	0.4	PCB	Low	DMSLs-RWG
[17]	110–138	Non-Galvanic Antenna	Plastic Mold 3.2	3†	22	1.25×1.08	0.19	eWLB	High	CPW-RWG
[18]	116–151	Slot Antenna with Si Taper	Plastic Mold 3.2	2.1	26	0.76×0.71	>1.16	eWLB	High	CPW-RWG
[20]	110–153	Tapered Slot	Mold Compound	2.8†	33	1.32×0.79	0.2	MEMS	Medium	SL-RWG
[20]	116–152	Matched Rectangular Ring Slot	Mold Compound	3.7†	27	1.29×0.85	0.2	MEMS	Medium	CPW-RWG
[21]	156–171	Radiation Patch with TGVs	B33 glass 4.29	2.85	9.17*	0.91×0.41#	0.49	LIDE	High (Multilayer)	MSL-SIW-DWG
[22]	155–167	Stacked Patch on Glass	B33 glass 4.29	2.95	7.4*	0.35×0.17#	>0.84	LIDE	High (Multilayer)	MSL-DWG
[22]	152–170	Ring Slot Patch with TGVs	B33 glass 4.29	2.62	10.8*	0.46×0.24#	>0.62	LIDE	High (Multilayer)	MSL-DWG
[23]	124–161	Cavity Coupling with EBG Structure	GaAs 12.9	0.8	26	>0.81×0.95#	>0.57	GaAs	Low	RWG-MSL-RWG
This work	140–155	Silicon-based Air Cavity-backed Structure	BCB 2.65 Silicon 11.6	1.1 (2.4†)	10.2	1.18×0.53	0.19	MEMS	Medium	GCPW-SIW-RWG

† The average insertion loss within the 3-dB bandwidth. * 1-dB-FBW.
# The footprint area in the vertical direction of the main radiation structure without the length of the transmission line or waveguide.
λ_0 represents the free space wavelength at the center of the operating bandwidth.
The abbreviations mentioned above are represented as FBW – fractional bandwidth; TGVs – through-glass vias; QFN – quad flat no-leads package; PCB – printed circuit board; MEMS – micro electromechanical systems; LIDE – laser-induced deep etching; CPW – coplanar waveguide; MSL – microstrip line; DMSLs – differential microstrip lines; SL – slot line; DWG – dielectric waveguide.

of the BCB-based GCPW is approximately 0.58 dB/mm at 145 GHz. The 20 mm GCPW is used to compensate and calculate the loss in the measurement of the back-to-back transition.

The back-to-back transition has a length of 20 mm GCPW with two extra length of 0.55 mm GCPW in the silicon-based air cavity-backed transitions at each side. Fig. 20 shows the comparisons between the simulated and measured results of the back-to-back transition. The surface roughness and the fabrication tolerance of the metal layer have been considered in the simulation. The measured minimum insertion loss is 13.8 dB at 147.5 GHz. Fig. 21 depicts that considering the measured insertion loss of the 20 mm GCPW shown in Fig. 19, the compensated minimum insertion loss of each silicon-based air cavity-backed transition is 1.1 dB, where it includes the 0.55 mm GCPW and 1.89 mm SIW-RWG structure. The 3-dB bandwidth is 15 GHz from 140 GHz to 155 GHz.

Table 2 presents the comparisons between our work and other state-of-the-art transitions. It can be found that a transition on a chip usually occupies more area. Further, PCB-based transition has a low insertion loss, however its profile is usually high [10]. MEMS or eWLB technology are used to reduce the profile while the the insertion loss is deteriorated because of high radiation [17], [20]. Our silicon-based air cavity-backed transition exhibits both low insertion loss (1.1 dB) and low profile (0.19λ0). This transition can be further used to 3D integrate with SOC and antenna.

VI. CONCLUSION

A D-band low-loss 3D silicon-based air cavity-backed transition is designed, fabricated, and measured. An equivalent circuit model is established, where detailed design procedures are given. The calculated, simulated, and measured S-parameters show some agreement. The minimum measured insertion loss is 1.1 dB at 147 GHz with 3-dB bandwidth of 10.2%. The average measured insertion loss is 2.4 dB within the passband. This transition demonstrates outstanding performance compared with that of state-of-the art works. It can be further interconnected with a D-band joint radar communication transceiver and antenna to demonstrate a system in packaging by using our in-house silicon-based MEMS photosensitive composite film fabrication process.

REFERENCES

[1] A. Visweswaran et al., "A 28-nm-CMOS based 145-GHz FMCW radar: System, circuits, and characterization," *IEEE J. Solid-State Circuits*, vol. 56, no. 7, pp. 1975–1993, Jul. 2021.

[2] W. A. Ahmad et al., "Multimode W-band and D-band MIMO scalable radar platform," *IEEE Trans. Microw. Theory Techn.*, vol. 69, no. 1, pp. 1036–1047, Jan. 2021.

[3] H. S. Son, T. H. Jang, S. H. Kim, K. P. Jung, J. H. Kim, and C. S. Park, "Pole-controlled wideband 120 GHz CMOS power amplifier for wireless chip-to-chip communication in 40-nm CMOS process," *IEEE Trans. Circuits Syst. II, Exp. Briefs*, vol. 66, no. 8, pp. 1351–1355, Aug. 2019.

[4] H. Li et al., "W-band scalable 2 × 2 phased-array transmitter and receiver chipsets in SiGe BiCMOS for high data-rate communication," *IEEE J. Solid-State Circuits*, vol. 57, no. 9, pp. 2685–2701, Sep. 2022.

[5] S. Hansen, C. Bredendiek, G. Briese, A. Froehly, R. Herschel, and N. Pohl, "A SiGe-chip-based D-band FMCW-radar sensor with 53-GHz tuning range for high resolution measurements in industrial applications," *IEEE Trans. Microw. Theory Techn.*, vol. 70, no. 1, pp. 719–731, Jan. 2022.

[6] S. Callender et al., "A fully integrated 160-Gb/s D-band transmitter achieving 1.1-pJ/b efficiency in 22-nm FinFET," *IEEE J. Solid-State Circuits*, vol. 57, no. 12, pp. 3582–3598, Dec. 2022.

[7] A. Bhutani, B. Goettel, T. Streitz, S. Scherr, W. Winkler, and T. Zwick, "Low-cost antenna-in-package solution for 122 GHz radar module," in *Proc. 46th Eur. Microw. Conf.*, Oct. 2016, pp. 1469–1472.

[8] J. Campion et al., "Toward industrial exploitation of THz frequencies: Integration of SiGe MMICs in silicon-micromachined waveguide systems," *IEEE Trans. THz Sci. Technol.*, vol. 9, no. 6, pp. 624–636, Nov. 2019.

[9] Y. Dong, V. Zhurbenko, P. S. Hanberg, and T. K. Johansen, "A D-band rectangular waveguide-to-coplanar waveguide transition using metal ridge," in *Proc. IEEE MTT-S Int. Microw. Symp.*, Boston, MA, USA, 2019, pp. 1050–1053.

[10] P. Hugler, T. Chaloun, and C. Waldschmidt, "A wideband differential microstrip-to-waveguide transition for multilayer PCBs at 120 GHz," *IEEE Microw. Wireless Compon. Lett.*, vol. 30, no. 2, pp. 170–172, Feb. 2020.

[11] A. Hassona et al., "Nongalvanic generic packaging solution demonstrated in a fully integrated D-band receiver," *IEEE Trans. THz Sci. Technol.*, vol. 10, no. 3, pp. 321–330, May 2020.

[12] M. Hörberg, J. Campion, J. Oberhammer, J. Hansryd, and Y. Li, "A 110–170-GHz non-galvanic interface for integrating silicon micromachined chips with metallic waveguide systems," *IEEE Trans. Microw. Theory Techn.*, vol. 69, no. 8, pp. 3667–3674, Aug. 2021.

[13] C. Wang, Y. Yao, J. Wang, X. Cheng, J. Yu, and X. Chen, "A wideband contactless CPW to W-band waveguide transition," *IEEE Microw. Wireless Compon. Lett.*, vol. 29, no. 11, pp. 706–709, Nov. 2019.

[14] I. Mohamed and A. Sebak, "Broadband transition of substrate integrated waveguide-to-air-filled rectangular waveguide," *IEEE Microw. Wireless Compon. Lett.*, vol. 28, no. 11, pp. 966–968, Nov. 2018.

[15] K. Zhu, Y. Xiao, W. Tan, H. Luo, and H. Sun, "A broadband E-band single-layer-SIW-to-waveguide transition for automotive radar," *IEEE Microw. Wireless Compon. Lett.*, vol. 32, no. 6, pp. 523–526, Jun. 2022.

[16] C.-H. Li and T.-Y. Chiu, "Low-loss single-band, dual-band, and broadband mm-wave and (sub-)THz interconnects for THz SoP heterogeneous system integration," *IEEE Trans. THz Sci. Technol.*, vol. 12, no. 2, pp. 130–143, Mar. 2022.

[17] A. Hassona et al., "A non-galvanic D-band MMIC-to-waveguide transition using eWLB packaging technology," in *Proc. IEEE MTT-S Int. Microw. Symp.*, 2017, pp. 510–512.

[18] A. Hassona, V. Vassilev, Z. S. He, C. Mariotti, F. Dielacher, and H. Zirath, "Silicon taper based D-band chip to waveguide interconnect for millimeter-wave systems," *IEEE Microw. Wireless Compon. Lett.*, vol. 27, no. 12, pp. 1092–1094, Dec. 2017.

[19] M. Frank et al., "Antenna and package design for 61- and 122-GHz radar sensors in embedded wafer-level ball grid array technology," *IEEE Trans. Microw. Theory Techn.*, vol. 66, no. 12, pp. 5156–5168, Dec. 2018.

[20] A. Hassona et al., "Demonstration of +100-GHz interconnects in eWLB packaging technology," *IEEE Trans. Compon., Packag. Manuf. Technol.*, vol. 9, no. 7, pp. 1406–1414, Jul. 2019.

[21] T. Galler et al., "Glass package for radar MMICs above 150 GHz," *IEEE J. Microwaves*, vol. 2, no. 1, pp. 97–107, Jan. 2022.

[22] T. Galler et al., "MMIC-to-dielectric waveguide transitions for glass packages above 150 GHz," *IEEE Trans. Microw. Theory Techn.*, vol. 71, no. 7, pp. 2807–2817, Jul. 2023.

[23] A. Hassona, V. Vassilev, A. U. Zaman, V. Belitsky, and H. Zirath, "Compact low-loss chip-to-waveguide and chip-to-chip packaging concept using EBG structures," *IEEE Microw. Wireless Compon. Lett.*, vol. 31, no. 1, pp. 9–12, Jan. 2021.

[24] L. Zhu et al., "3-D printed rectangular waveguide 123–129 GHz packaging for commercial CMOS RFICs," *IEEE Microw. Wireless Technol. Lett.*, vol. 33, no. 2, pp. 157–160, Feb. 2023.

[25] X.-L. Huang, L. Zhou, Y. Yuan, L.-F. Qiu, and J.-F. Mao, "Quintuple-mode W-band packaged filter based on a modified quarter-mode substrate-integrated waveguide cavity," *IEEE Trans. Compon., Packag. Manuf. Technol.*, vol. 9, no. 11, pp. 2237–2247, Nov. 2019.

[26] L. Yang, Y. Yuan, and L. Zhou, "Low loss W-band packaged filtering balun based on a modified quarter-mode folded substrate-integrated waveguide cavity," *IEEE Access*, vol. 10, pp. 64339–64347, 2022.

[27] Y.-S. Huang et al., "A 1T2R heterogeneously integrated phased-array FMCW radar transceiver with AMC-based antenna in package in the W-band," *IEEE Trans. Microw. Theory Techn.*, vol. 72, no. 6, pp. 3772–3787, Jun. 2024, doi: 10.1109/TMTT.2023.3328482.

[28] Y.-S. Huang, L. Zhou, Q.-H. Xu, and J.-F. Mao, "A W-band self-packaged SIW-based slot antenna with gain and bandwidth enhancement," *IEEE Trans. Antennas Propag.*, vol. 71, no. 3, pp. 2158–2166, Mar. 2023.

[29] X. Yang et al., "Low-loss heterogeneous integrations with high output power radar applications at W-band," *IEEE J. Solid-State Circuits*, vol. 57, no. 6, pp. 1563–1577, Jun. 2022.

[30] Z. Zhang, Y. Huang, and L. Zhou, "A D-band GCPW to SIW to air-filled RWG cavity-backed transition for integration of communication system," in *Proc. 10th Asia-Pacific Conf. Antennas Propag.*, 2022, pp. 1–2.

[31] W. Deng et al., "A D-band joint radar-communication CMOS transceiver," *IEEE J. Solid-State Circuits*, vol. 58, no. 2, pp. 411–427, Feb. 2023.

[32] J. X. Sun, Y. J. Cheng, L. Wang, and Y. Fan, "Three-dimensional interconnection with magnetically coupled transition for W-Band integration applications," *IEEE Trans. Microw. Theory Techn.*, vol. 71, no. 1, pp. 112–121, Jan. 2023.

[33] J.-S. Hong, *Microstrip Filters for RF/Microwave Applications*. Hoboken, NJ, USA: Wiley, 2001.

[34] K.-F. Lee, K. Ho, and J. Dahele, "Circular-disk microstrip antenna with an air gap," *IEEE Trans. Antennas Propag.*, vol. 32, no. 8, pp. 880–884, Aug. 1984.